

Inverse response of $^{231}\text{Pa}/^{230}\text{Th}$ to variations of the Atlantic Meridional Overturning Circulation in the North Atlantic intermediate water

Finn Süfke^{1*}, Hartmut Schulz², Jeemijn Scheen^{3,4}, Sönke Szidat^{4,5}, Marcel Regelous⁶, Patrick Blaser¹, Frerk Pöppelmeier¹, Tyler J. Goepfert^{7,8}, Thomas F. Stocker^{3,4} and Jörg Lippold¹

¹Heidelberg University, Institute of Earth Sciences, Heidelberg, Germany

²University of Tübingen, Institute of Earth Sciences, Tübingen, Germany

³University of Bern, Climate and Environmental Physics, Physics Institute, Bern, Switzerland

⁴University of Bern, Oeschger Centre for Climate Change Research, Bern, Switzerland

⁵University of Bern, Department of Chemistry and Biochemistry, Bern, Switzerland

⁶FAU Erlangen-Nürnberg, GeoZentrum Nordbayern, Erlangen, Germany

⁷GEOMAR Helmholtz-Center for Ocean Research Kiel, Kiel, Germany

⁸Arizona State University, School of Earth and Space Exploration, Tempe, AZ, USA

*corresponding author: finn.suefke@geow.uni-heidelberg.de / Tel.: +496221546063

ORCID: 0000 0001 5271 1099

Abstract

This study aims to provide a more detailed understanding of the behavior of $^{231}\text{Pa}/^{230}\text{Th}$ under varying ocean circulation regimes. The North Atlantic provides a unique sedimentary setting with its Ice-Rafted-Detritus (IRD) layers deposited during glacial times. These layers have been found north of 40°N (Ruddiman Belt) and are most pronounced during Heinrich Stadials. Most of these sediments have been recovered from the deep North Atlantic basin typically below 3000 m water depth. This study reports sedimentological and sediment geochemical data from one of the few sites at intermediate depth of the open North Atlantic (core SU90-I02, 45°N 39°W, 1965 m water depth) within the Ruddiman Belt. The time periods of Heinrich Stadials 1 and 2 of this core were identified with the help of the major element composition by XRF scanning and by IRD counting. Along the core profile the sedimentary $^{231}\text{Pa}/^{230}\text{Th}$ activity ratio has been measured as a kinematic proxy for the circulation strength. The $^{231}\text{Pa}/^{230}\text{Th}$ record shows highest values during the Holocene and LGM, above the natural production ratio of these isotopes. During Heinrich Stadial 1 and 2, when AMOC was most reduced, the $^{231}\text{Pa}/^{230}\text{Th}$ record shows overall lowest values below the production ratio. This behavior is contrary to classical findings of $^{231}\text{Pa}/^{230}\text{Th}$ from the northwestern Atlantic where a strong Holocene circulation is associated with low values. However, this behavior at the presented location is in agreement with results from simulations of the $^{231}\text{Pa}/^{230}\text{Th}$ -enabled Bern3D Earth System Model.

38 **1. Introduction**

39 Changes in the paleoclimate of the North Atlantic region have been related to variations in the Atlantic
40 Meridional Overturning Circulation (AMOC) on glacial-interglacial down to millennial scale timescales
41 as observed from deep marine sediments (e.g. Lynch-Stieglitz, 2017). One example of the sedimentary
42 features of the North Atlantic is the episodic occurrence of distinguished layers of terrigenous
43 sediments ranging from detrital carbonate to cm-wide clastic rocks in sediments north of 40°N
44 (Ruddiman Belt; Ruddiman, 1977). These prominent sediment layers are associated with discharge-
45 events of icebergs originated from the Labrador Sea and are known as Ice Rafted Detritus (IRD) or
46 Heinrich layers (Heinrich, 1988; Andrews and Tedesco, 1992; Bond et al., 1992; Broecker et al., 1992;
47 Hemming, 2004). Heinrich layers have been the target of a great amount of studies aiming for
48 understanding their origin, climatic background and consequence (Heinrich, 1988; Andrews and
49 Tedesco, 1992; Bond et al., 1992; Broecker et al., 1992; Grousset et al., 2001; Hemming, 2004, Rashid
50 and Boyle, 2007; Hodell et al., 2008; Bradtmiller et al., 2014; Hodell et al., 2017, Andrews and Voelker,
51 2018). Most paleoclimatologic studies agree that Heinrich layers are associated with Heinrich Stadials,
52 climate periods on millennial scales with an extraordinary cold and dry climate. Large inputs of
53 freshwater into the North Atlantic are a common feature of Heinrich Stadials (e.g. Duplessy et al., 1992;
54 Clark et al., 2001; Roche et al., 2004). Since the North Atlantic region and its adjacent seas are key
55 regions for the AMOC with their deep water formation zones, the AMOC is highly sensitive to abrupt
56 changes by e.g. freshwater input into the area (McManus et al., 2004). One consequence is the
57 reorganization of water mass distributions in the Atlantic during Heinrich Stadials (e.g. Henry et al.,
58 2016).

59 The reconstruction of changes in AMOC strength is often enabled with the kinematic circulation
60 strength proxy $^{231}\text{Pa}/^{230}\text{Th}_{(xs,0)}$. The radioisotopes ^{231}Pa and ^{230}Th are the radioactive decay products of
61 ^{235}U and ^{234}U , respectively. Uranium is homogeneously dissolved in the world ocean and decays to ^{231}Pa
62 and ^{230}Th at a constant activity ratio of 0.093 (so called “production ratio”; Henderson and Anderson,
63 2003). In contrast to uranium, protactinium and thorium are highly particle-reactive elements with
64 residence times in the range of ~150 and ~20 years, respectively (Henderson and Anderson, 2003). The
65 higher residence time of protactinium is caused by its lower affinity to particles in the water column,
66 compared to thorium. The resulting fractionation, due to particle reactivity, is the key process of the
67 $^{231}\text{Pa}/^{230}\text{Th}$ proxy. While ^{230}Th is virtually scavenged completely from the water column after
68 production, ^{231}Pa can be laterally advected by deep water currents on a basin scale. Therefore, high
69 ratios indicate slow circulation and vice versa. Accordingly, $^{231}\text{Pa}/^{230}\text{Th}$ is anti-correlated with the basin-
70 scale circulation strength (e.g. Yu et al., 1996; McManus et al., 2004). However, protactinium shows a
71 high affinity to biogenic opal (Chase et al., 2003), which acts as an effective sink for protactinium (e.g.
72 in the Southern Ocean; Rutgers van der Loeff et al., 2016) potentially obscuring its circulation signal.

73 Furthermore, the usage of the $^{231}\text{Pa}/^{230}\text{Th}$ proxy is complicated in regions of high particle fluxes and
74 weak deep water advection such as ocean margins (Anderson et al., 1983; Hayes et al., 2015a). In
75 contrast, the role of Ice Rafted Detritus (IRD) and lithogenic particles in general is thought to be of
76 minor importance on the scavenging behavior of ^{231}Pa (Chase et al., 2002,2004; Roberts et al., 2014).

77 The expected anti-correlated response of $^{231}\text{Pa}/^{230}\text{Th}$ to AMOC strength has been demonstrated by
78 several model approaches (Gu and Liu, 2017; Marchal et al., 2000; Siddall et al., 2007; Rempfer et al.,
79 2017), and represents a general feature in the deep West Atlantic (McManus et al., 2004; Gherardi et
80 al., 2005; Bradtmiller et al., 2007; Gherardi et al., 2009; Lippold et al., 2012a; Bradtmiller et al., 2014;
81 Böhm et al., 2015; Henry et al., 2016; Lippold et al., 2016; Mulitza et al., 2017; Voigt et al., 2017; Ng et
82 al., 2018; Waelbroeck et al., 2018; Süfke et al., 2019). However, a number of downcore profiles from
83 the shallower North Atlantic give a different picture of high $^{231}\text{Pa}/^{230}\text{Th}$ during the Holocene despite its
84 evident strong export of North Atlantic Deep Water (NADW) (Hall et al., 2006; Gherardi et al., 2009;
85 Lippold et al., 2012a, 2012b, 2016) and therefore the generally accepted notion of a pronounced ^{231}Pa
86 export (Deng et al., 2018). This contradictory behavior, however, has been already predicted for the
87 shallower northern North Atlantic by models of simple and intermediate complexity (Luo et al., 2010;
88 Rempfer et al., 2017). In particular, Rempfer et al. (2017) noted that the area north of $\sim 40^\circ\text{N}$ and above
89 2500 m water depth is supposed to show a positive correlation between $^{231}\text{Pa}/^{230}\text{Th}$ and AMOC
90 strength based on the Bern3D model.

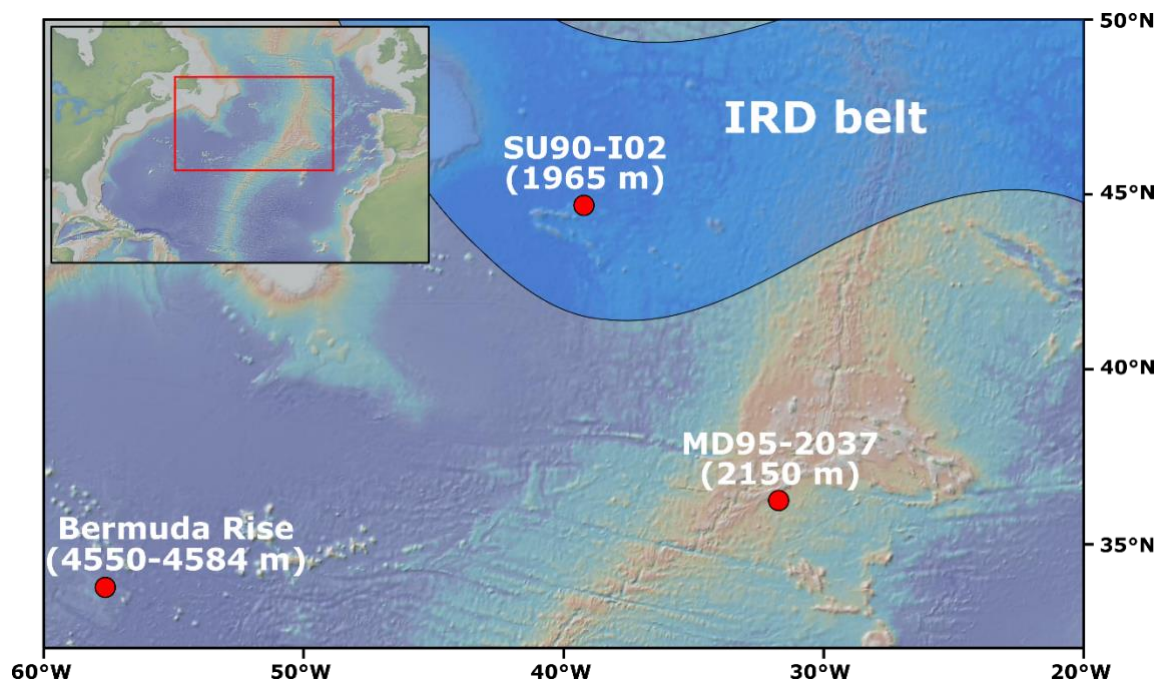
91 This study aims to provide a deeper understanding of the relation between $^{231}\text{Pa}/^{230}\text{Th}$ and AMOC
92 strength variations by presenting a new $^{231}\text{Pa}/^{230}\text{Th}$ downcore profile from the mid-depth North
93 Atlantic at 45°N . The $^{231}\text{Pa}/^{230}\text{Th}$ profile is complemented by foraminifera abundance data and the
94 information of the sedimentary composition by XRF scanning, IRD counting and biogenic opal content
95 that were analyzed to identify and investigate the impact of climate events like Heinrich Stadial 1 and
96 2 on the research area.

97 **2. Methods and Material**

98 **2.1. Core location and age model**

99 In this study sediments from interface core SU90-I02 with a total length of 43 cm on top of one of the
100 easternmost Milne Seamounts ($45^\circ 05' \text{ N}$, $39^\circ 26' \text{ W}$) at 1965 m water depth were analyzed (Fig. 1). The
101 Milne Seamounts are located in the open North Atlantic east from the Grand Banks of Newfoundland.
102 The investigated site lies within the Ruddiman Belt (Ruddiman, 1977) and sediments deposited before
103 the Holocene are therefore characterized by high amounts of IRD. Today the core site is bathed by
104 Labrador Sea Water which is part of southward flowing NADW (Ferreira and Kerr, 2017).

105 The general core chronology is based on the correlation of the $\delta^{18}\text{O}$ record to other records of the
106 North Atlantic region (Fig. S2) and was refined by four ^{14}C Accelerator Mass Spectrometry (AMS) dates.
107 The new radiocarbon-based age tie-point dates have been measured at the LARA laboratory at the
108 University of Bern, Switzerland (Szidat et al., 2014; Gottschalk et al., 2018). The CALIB 7.1 online tool
109 tied to the Marine13 calibration curve was used (Reimer et al., 2013) with a 400 year reservoir age
110 correction (Table S1).



112 **Fig. 1** Overview map of the northern North Atlantic region with the position of core SU90-I02 (45°05'N 39°26'W) on the
113 Milne Seamounts, MD95-2037 (37°05'N 32°01'W; Gherardi et al., 2009) and the Bermuda Rise site (OCE329-GGC5: 33°42'N
114 57°35'W, McManus et al., 2004; ODP 1063: 33°41'N 57°37'W, Lippold et al., 2009). Number in brackets indicate the water
115 depth of the sites. The blue shaded area depicts the main area of IRD depositions during Heinrich Events 1 and 2 (after
116 Hemming, 2004).

117 **2.2. Analytical methods**

118 The light-colored sandy sediments of interface core SU90-I02 were first sampled continuously in July
119 1990 on board of the research vessel Le Suroit at 2 cm intervals down to 42.5 cm core depth. These
120 samples were used for investigation of the foraminifera assemblage, stable isotope analyses,
121 radiocarbon dating and IRD counting on the washed sand fraction. Later in 2018, the last available
122 series of bulk sediment samples was collected from Bordeaux University (EPOC) for sedimentary
123 $^{231}\text{Pa}/^{230}\text{Th}$, XRF and opal analysis (Table S1). This sample series covers continuously the whole core
124 but with discontinuous sample widths up to 2.5 cm (Table S1). Sample splits from the first sample series
125 for planktic foraminifera analyses were freeze-dried, wet-sieved over a 63 μm screen, and oven-dried
126 at 40°C. Counts were conducted on the whole residue or on splits of the size fraction $>150 \mu\text{m}$ and
127 examined under a stereo-dissecting microscope in order to obtain the sand fraction of $>150 \mu\text{m}$ and
128 to quantify the inorganic (IRD counts) and microfossil (foraminifera) components. Planktic foraminifera

129 were identified to the species level (Banner and Blow, 1960; Bandy, 1972; Kucera, 2007; Storz et al.,
130 2009; Schiebel and Hemleben, 2017). Foraminifera samples of *Neogloboquadrina pachyderma sinistral*
131 were cracked and cleaned with methanol in an ultra-sonic bath before $\delta^{18}\text{O}$ analysis. The $\delta^{18}\text{O}$ analysis
132 (Schulz, 1995b) were carried out in the former Institute for Pure and Applied Nuclear Physics at the
133 University of Kiel, Germany.

134 Separation and purification of protactinium, uranium and thorium isotopes from sediment samples of
135 SU90-I02 followed the protocol described by Sufke et al. (2018). Samples were spiked with ^{229}Th , ^{236}U
136 and ^{233}Pa before total dissolution in a mixture of concentrated HCl, HNO_3 and HF, which was then
137 followed by further chemical purification by column chromatography. Since ^{233}Pa is a short lived
138 isotope ($t_{1/2} = 27$ d) it had been milked from a ^{237}Np solution (Regelous et al., 2004) directly before the
139 chemical treatment and purification of the samples. The ^{233}Pa spike was calibrated against the
140 reference materials UREM-11 (Sufke et al., 2018), IAEA-385 (Pham et al., 2008) and an internal
141 pitchblende standard (Fietzke et al., 1999). Finally, concentrations of the radioisotopes ^{230}Th , ^{231}Pa ,
142 ^{232}Th , ^{234}U , and ^{238}U were measured with a Neptune Plus MC-ICP-MS at the Geozentrum Nordbayern
143 in Erlangen, Germany.

144 For the calculation of $^{231}\text{Pa}_{\text{excess}}$ and $^{230}\text{Th}_{\text{excess}}$ from measured bulk ^{231}Pa and ^{230}Th a detrital correction
145 of $^{238}\text{U}/^{232}\text{Th} = 0.55$ has been applied (Henderson and Anderson, 2003). This correction is in agreement
146 with the overall minimum of bulk $^{238}\text{U}/^{232}\text{Th}$ in the samples of SU90-I02 and within typical lithogenic
147 activity ratios (0.5 to 0.6) found in the western Atlantic sector (Henderson and Anderson, 2003).
148 Variations in the detrital correction do not show a significant effect on the age corrected sedimentary
149 $^{231}\text{Pa}/^{230}\text{Th}_{\text{excess}}$ record (Lippold et al., 2016; Missiaen et al., 2018; Fig. S1) even for time periods of
150 distinctly different sedimentation regimes (e.g. Heinrich Events). This argues in favor of a negligible
151 impact of the lithogenic particle flux on the resulting $^{231}\text{Pa}/^{230}\text{Th}_{\text{excess}}$ record. ^{231}Pa and ^{230}Th excess
152 concentrations were decay corrected to the time of deposition. All individual isotope concentrations
153 are provided in the supplement (Table S1).

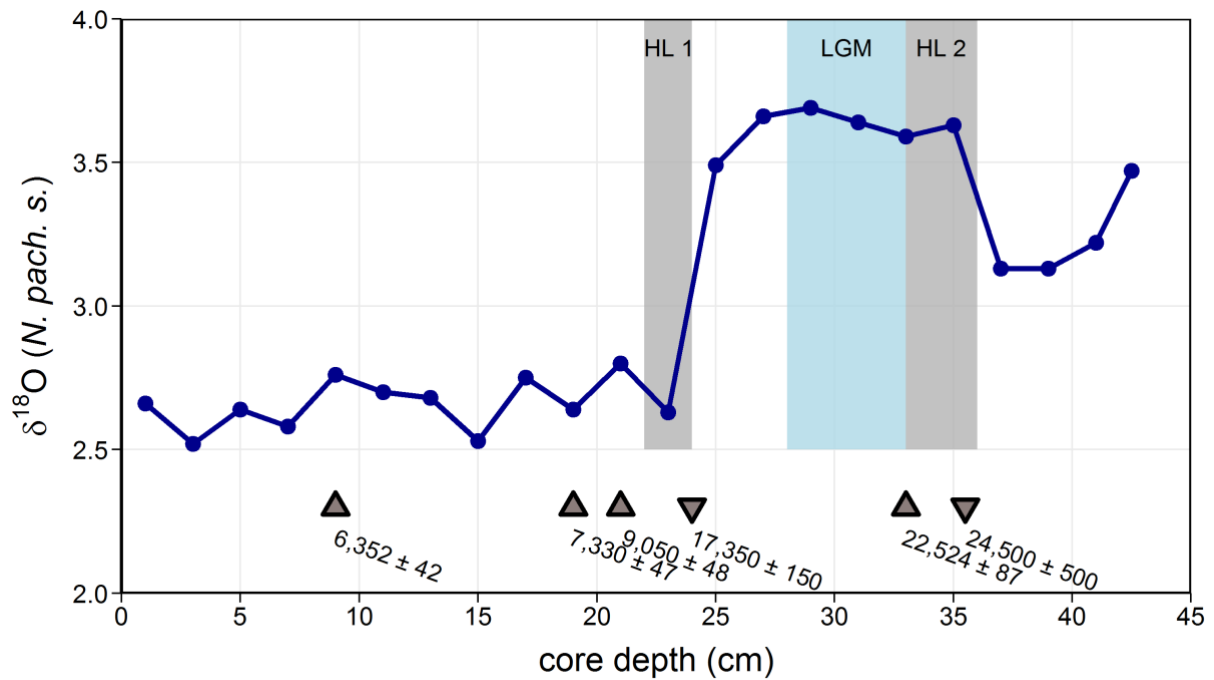
154 To investigate the potential influence of biogenic opal on ^{231}Pa (Chase et al., 2002, 2003; Rutgers van
155 der Loeff et al., 2016) the sedimentary opal concentration was analyzed by automated leaching
156 following the procedure described by Muller and Schneider (1993). Furthermore, the major element
157 composition (Al, Si, K, Ca, Ti and Sr) of discrete bulk sediment samples were analyzed with a fourth
158 generation Avaatech XRF core scanner at the Institute of Earth Sciences at Heidelberg University,
159 Germany. Elemental ratios (e.g. Ca/Sr) are a useful tool to identify Heinrich-Layers in the North Atlantic
160 (Hodell et al., 2008).

161 **3. Results**

162 **3.1. Age model refinement by ^{14}C and $\delta^{18}\text{O}$**

163 The core chronology was established for SU90-I02 based on stable oxygen isotope data (Schulz, 1995b),
164 as well as on four ^{14}C dates. The radiocarbon dates at sediment depths of 21 and 33 cm were obtained
165 from *N. pachyderma s.* and give absolute ages of 9 and 22.5 ka BP, respectively. Radiocarbon dates
166 from sediment depths 9 and 19 cm were obtained from *Globigerina bulloides* and give absolute ages
167 of 6.3 and 7.3 ka BP, respectively (Fig. 2; Table S1). A potential negative influence of analyzing different
168 species for radiocarbon dating on the accuracy of the age model is possible but has been found not to
169 be significant for the here investigated species and time periods (Manighetti et al., 1995). For a further
170 refinement of the age model the planktonic $\delta^{18}\text{O}$ record of *N. pachyderma s.* (Schulz, 1995b) was
171 correlated to established $\delta^{18}\text{O}$ records from the North Atlantic IRD belt (Bond et al., 1992; Labeyrie et
172 al., 1995; Grousset et al., 2001; Jullien et al., 2006; Rashid and Boyle, 2007; Hodell et al., 2017; Fig. S2).
173 All records from the before mentioned studies show a consistent picture of a shift in planktic $\delta^{18}\text{O}$
174 (from *N. pachyderma s.*) to lighter values between 17 and 17.5 ka right before the major IRD
175 depositions of Heinrich Stadial 1, as seen at 24 cm core depth in SU90-I02 (Fig. 2). Further, the slight
176 shift from lighter to heavier $\delta^{18}\text{O}$ at 35 cm in SU90-I02 can be correlated to a similar shift in $\delta^{18}\text{O}$
177 observed in the North Atlantic during Heinrich Stadial 2 between 24 and 25 ka (Broecker et al.,
178 1990/1992; Jullien et al., 2006; Rashid and Boyle, 2007). The increase in $\delta^{18}\text{O}$ in the deeper part of the
179 presented record can be related to a warm phase between Heinrich Stadial 2 and 3 (Heinrich 1988;
180 Broecker et al., 1990; Bond et al., 1992).

181 With these age constraints a hiatus in SU90-I02 is apparent in the depth below 21 cm (Fig. S3). While
182 the onset of Heinrich Layer 1 is present at 24 cm (see section 4.1.) the late Heinrich Stadial 1, the
183 Younger Dryas, the Bølling/Allerød and the very early Holocene parts are missing (Fig. S3). Additionally,
184 it has to be kept in mind that the exact timing and duration of SU90-I02 variations in $^{231}\text{Pa}/^{230}\text{Th}$ and
185 XRF samples are less well defined since these samples integrate up to 2.5 cm of sediment (Table S1).
186 Sample widths of 2.5 cm can integrate up to 1000 years in SU90-I02 and therefore limit the time
187 resolution.



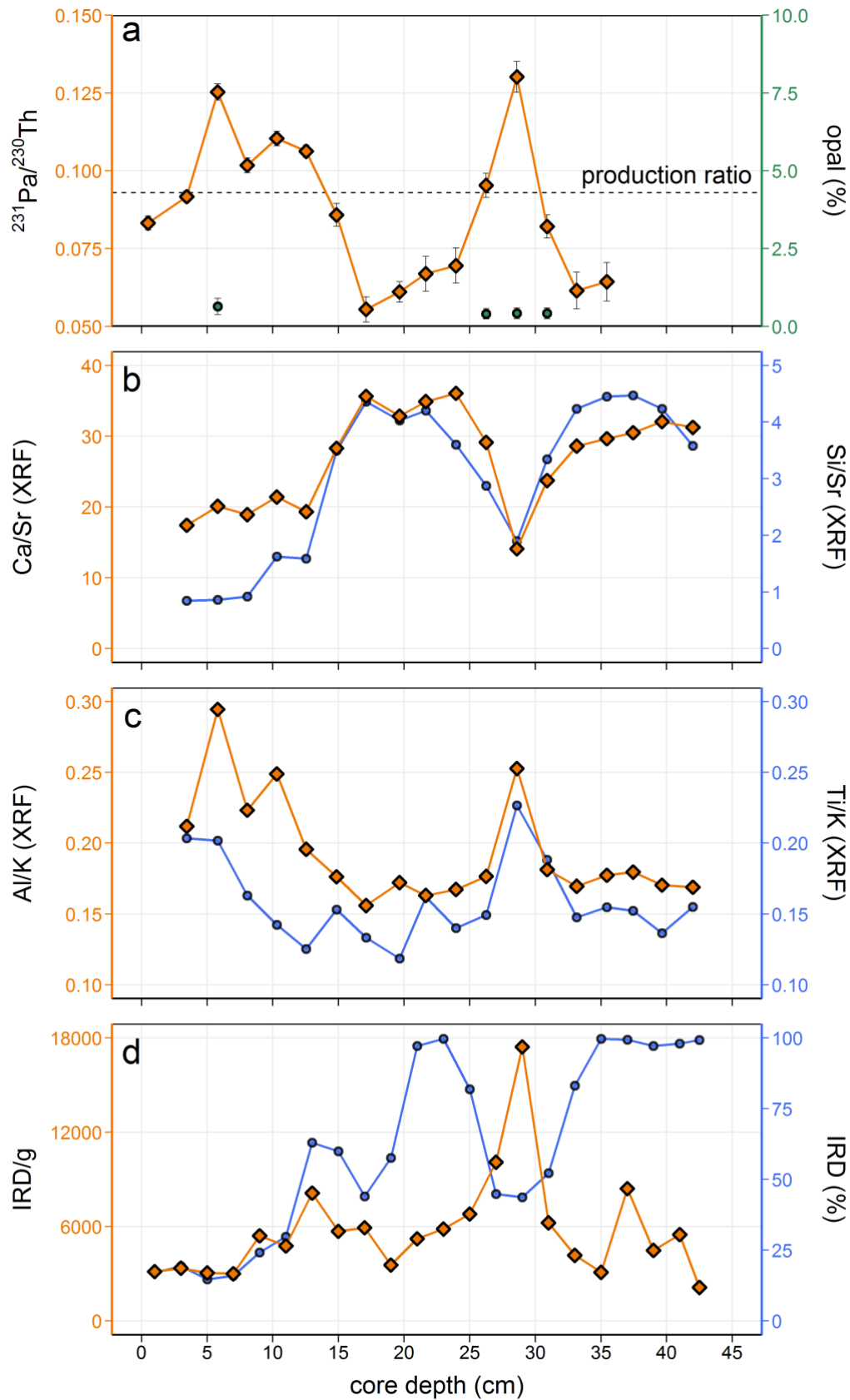
188

189 **Fig. 2** The $\delta^{18}\text{O}$ record of the planktic foraminifera *N. pachyderma s.* (Schulz, 1995b). Upward triangles indicate ^{14}C dates and
 190 downward triangle age tie points derived from $\delta^{18}\text{O}$ (cf. section 3.1.). Gray bars show the position of Heinrich Layers 1 (HL
 191 1) and 2 (HL 2) (based on IRD and foraminifera data; see Fig. 3, 4) and the blue bar indicate the Last Glacial Maximum (LGM)
 192 section of SU90-I02.

193

194 **3.2. Radioisotope analysis**

195 The $^{231}\text{Pa}/^{230}\text{Th}$ profile for SU90-I02 displays high values between 0.083 and 0.116 in the upper 15 cm
 196 of the core corresponding to the Holocene period (Fig. 3a). Further, at 29 cm core depth a sharp peak
 197 in $^{231}\text{Pa}/^{230}\text{Th}$ reaches 0.130, which is the highest value of the entire record, and is related to the LGM.
 198 Between 17 and 24 cm and below 33 cm $^{231}\text{Pa}/^{230}\text{Th}$ values are quite stable between 0.06 and 0.07.
 199 These intervals are related to the early Holocene as well as Heinrich Stadials 1 and 2, respectively.



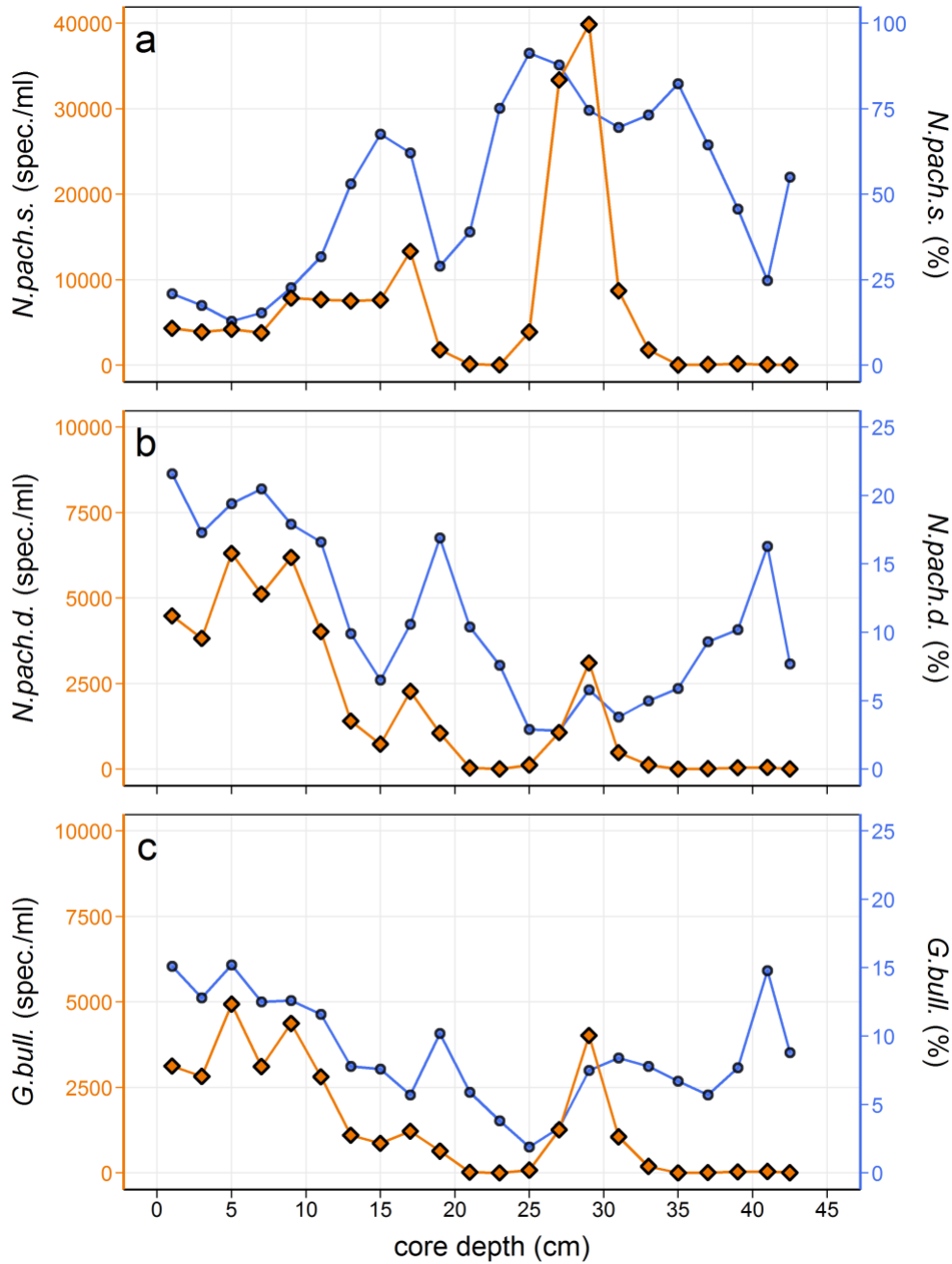
200

201 **Fig. 3** Geochemical and sedimentary parameters of SU90-I02. (a) $^{231}\text{Pa}/^{230}\text{Th}$ activity ratios and opal concentration (%). The
 202 dashed line indicates the production ratio of $^{231}\text{Pa}/^{230}\text{Th}$. (b, c) Bulk element ratios of Ca/Sr, Si/Sr, Al/K and Ti/K measured
 203 on discrete sediment samples by XRF. (d) Absolute IRD counts of the bulk sediment and relative IRD percentages in the
 204 $>150\ \mu\text{m}$ fraction.

205 **3.3. Sedimentary analysis of foraminifera, opal and major elements**

206 Planktic foraminifera of the species *Neogloboquadrina pachyderma sinistral*, *Neogloboquadrina*
207 *pachyderma dextral* (also called *Neogloboquadrina incompta*; Schiebel and Hemleben, 2017) and
208 *Globigerina bulloides* were investigated for this study (Fig. 4a/b/c) as representatives for a
209 colder/glacial (*N. pachyderma s.*) and more moderate (*N. pachyderma d.* and *G. bulloides*) environment
210 (e.g. Manighetti et al., 1995). Species *N. pachyderma d.* and *G. bulloides* show their highest abundances
211 in the top 10 cm of the core. Below 10 cm, *N. pachyderma s.* is the dominant species throughout the
212 record. In the interval between 19 and 25 cm core depth (including Heinrich Stadial 1) all species show
213 an abundance minimum (e.g. Heinrich, 1988). The following interval between 25 and 33 cm (LGM) is
214 characterized by the reappearance of all species. While *N. pachyderma d.* and *G. bulloides* reached
215 Holocene levels at 29 cm, *N. pachyderma s.* is the most dominant species with a relative abundance of
216 75 % of all foraminifera (Fig. 4a). Below 33 cm all species vanish again to extremely low abundance
217 rates (Heinrich Stadial 2).

218 The sedimentary composition is monitored by major element analysis as well as opal concentration
219 measurements and IRD counts (Fig 3; Table S1). Opal concentrations are constantly very low (< 1 %)
220 throughout the presented record (Fig. 3a). In contrast, major element ratios show a distinct pattern.
221 Ca/Sr and Si/Sr ratios are low in the top 17 cm of the core. Between 17 and 26 cm (including Heinrich
222 Stadial 1) highest values of these ratios are found. At 29 cm (LGM) both ratios return to low values as
223 seen during the Holocene. Below 29 cm ratios for Ca/Sr and Si/Sr return again to higher values like
224 seen during Heinrich Stadial 1. The lithogenic element ratios Al/K and Ti/K show high values in the top
225 7 cm, which then decrease to the overall lowest ratios in the interval downcore to 26 cm. At 29 cm
226 both lithogenic element ratios return to Holocene-like values but sharply decrease back to low ratios
227 below. The course of the XRF measurements is mirrored by the IRD counts (Fig. 3d). During intervals
228 of high Ca/Sr ratios (21 to 25 and 35 to 42 cm) the percentage of IRD in the >150 µm fraction is nearly
229 100 %. Lowest IRD percentages are visible in the top 10 cm of the core (Holocene) and around 29 cm
230 (LGM). The timing of these periods matches the most pronounced changes in the XRF data,
231 abundances of investigated foraminifera species and $^{231}\text{Pa}/^{230}\text{Th}$.



232

233 **Fig. 4** Absolute (orange; in specimens per ml) and relative (blue; in % of all foraminifera; Schulz, 1995b) abundances of the
 234 foraminifera species *N. pachyderma s.* (a), *N. pachyderma d.* (b), and *G. bulloides* (c). Please note the different y-scale for
 235 panel a compared to panels b and c.

236 **4. Discussion**

237 **4.1. Characterization of Heinrich layers**

238 The core chronology is extended by the identification of Heinrich layers in SU90-I02. Heinrich layers
 239 are characterized by detrital carbonate which can easily be identified in North Atlantic sediments by
 240 its high Ca/Sr signature compared to regular marine sediments (Hodell et al., 2008). In SU90-I02 highest
 241 Ca/Sr ratios were identified in the depth interval between 15 and 25 cm as well as below 30 cm down
 242 to 42 cm (Fig. 3b). The course of Ca/Sr is also reflected in Si/Sr, which indicates the presence of silicate-

243 rich IRDs (Hodell et al., 2008; Fig. 3b). Accompanied by the relative amount of IRD in the >150 μm
244 fraction (IRD %; Fig. 3d), with highest values of nearly 100 % of IRD between 21 and 25 cm as well as
245 below 33 cm, both these intervals can be assigned to Heinrich Layers 1 and 2, respectively. Both
246 Heinrich layers are interrupted by a sharp decrease in Ca/Sr and Si/Sr at 29 cm (LGM) which occurs at
247 the same interval as absolute foraminifera abundance as well as the $^{231}\text{Pa}/^{230}\text{Th}$ record are increased.
248 The low Ca/Sr can be interpreted as absent detrital carbonate and a sediment source different from
249 Heinrich-IRDs inferred from low Si/Sr (Hodell et al., 2008; Hodell et al., 2017). Further, the ratios of the
250 terrigenous elements (Ti/K and Al/K) show an anomaly at the same core depth (Fig. 3c). IRD deposits
251 during Heinrich Events can be linked to a North Canadian source (e.g. Andrews and Tedesco, 1992),
252 while IRDs during the LGM most likely originated from Greenland (Watkins et al., 2007). Additionally,
253 absolute IRD counts are highest at the core depth of 29 cm, while the relative amount of IRD in the
254 >150 μm fraction is much lower (~44 %) than in Heinrich layers. The lower concentrations of IRD during
255 the LGM is the effect of the high abundances of preserved foraminifera diluting the IRD in the >150
256 μm fraction. In contrast, during Heinrich Stadial 1 and 2 foraminifera are nearly absent in the >150 μm
257 fraction (Fig. 4) caused either by an environment not favorable for foraminifera growth or a massive
258 dilution of foraminifera shells in the sediment by IRDs.

259 **4.2. The role of particle flux on $^{231}\text{Pa}/^{230}\text{Th}$ at SU90-I02**

260 The new $^{231}\text{Pa}/^{230}\text{Th}$ downcore profile of SU90-I02 displays high Holocene values, above production
261 ratio, preceded by lower values during the intervals of the Heinrich Stadial 1 and 2 interrupted by a
262 distinctive peak of high $^{231}\text{Pa}/^{230}\text{Th}$ during the LGM (Fig. 3a). The high sedimentary $^{231}\text{Pa}/^{230}\text{Th}$ above
263 the production ratio from a North Atlantic sediment core during the Holocene calls at first glance for a
264 strong influence of particle flux and/or particle composition on protactinium-scavenging (Anderson et
265 al., 1983; Christl et al., 2010). However, preserved opal concentrations, known as an effective
266 scavenger of protactinium (Chase et al., 2003; Rutgers van der Loeff et al., 2016), are low during the
267 Holocene and LGM (Fig. 3a) and thus clearly below the range (>5-10 %) for which any empirical
268 correlation between opal and increased $^{231}\text{Pa}/^{230}\text{Th}$ values can be observed in the Atlantic (Lippold et
269 al., 2012a; Ng et al., 2018).

270 Further, the ^{230}Th normalized sediment flux is lowest when $^{231}\text{Pa}/^{230}\text{Th}$ is highest and vice-versa (Fig. 5)
271 arguing against a major influence of particle flux on the temporal evolution of the $^{231}\text{Pa}/^{230}\text{Th}$ record.
272 This observation is further corroborated by the ^{230}Th normalized vertical sediment-accumulation rate
273 of around 3 to 7 $\text{g}/\text{cm}^2/\text{ka}$ for the time periods of highest $^{231}\text{Pa}/^{230}\text{Th}$. Similar vertical fluxes have been
274 reported from sites of circulation dominated $^{231}\text{Pa}/^{230}\text{Th}$ records (McManus et al., 2004; Gherardi et
275 al., 2009; Roberts et al., 2014). Roberts et al. (2014) also conclude that fluxes of ~5 $\text{g}/\text{cm}^2/\text{ka}$ are not
276 capable of significantly increasing the $^{231}\text{Pa}/^{230}\text{Th}$ ratio in a circulation controlled setting. Interestingly,

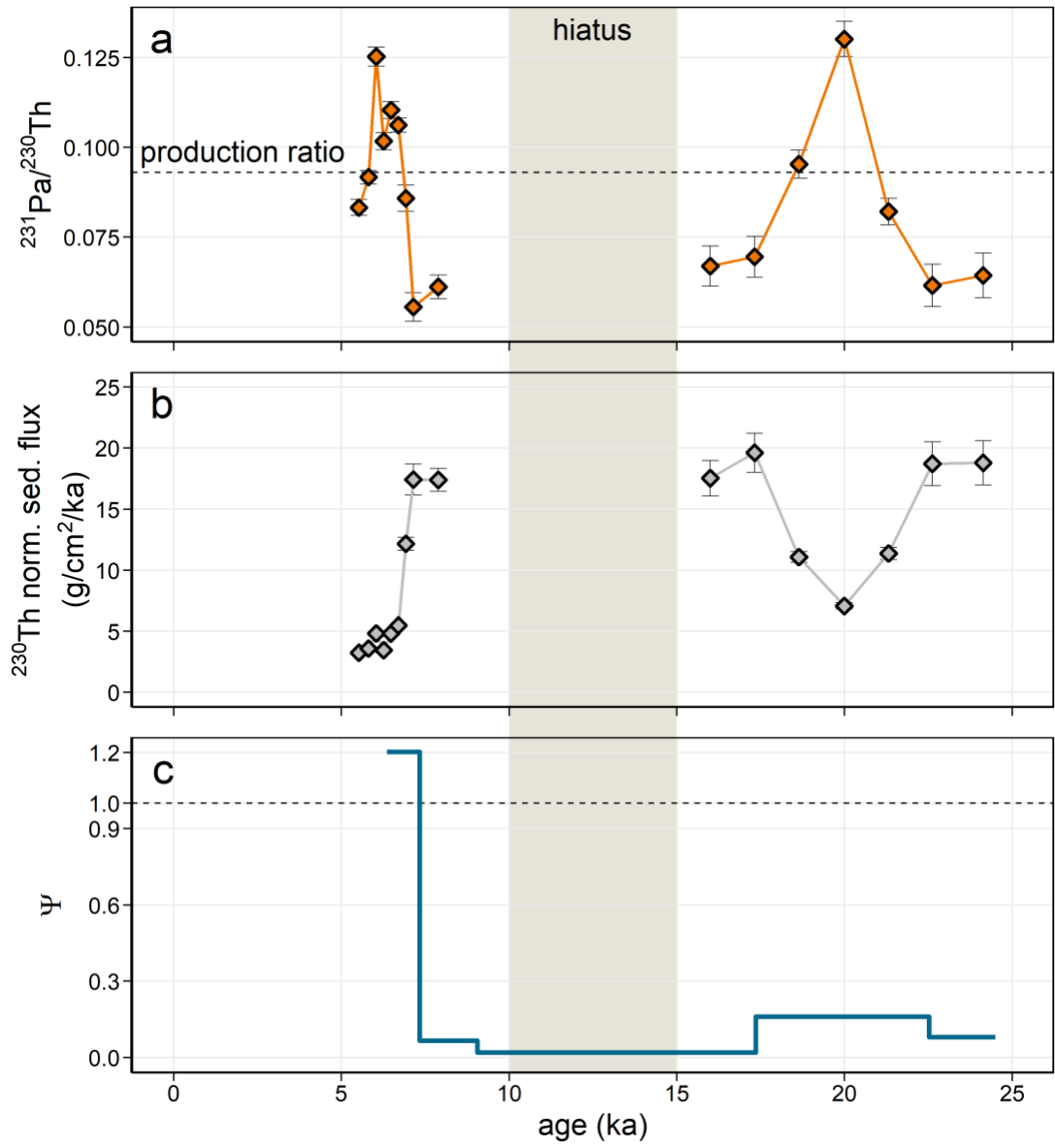
277 when the ^{230}Th normalized sediment flux is greatest, reaching values up to $20 \text{ g/cm}^2/\text{ka}$, $^{231}\text{Pa}/^{230}\text{Th}$ is
278 lowest with values clearly below the production ratio. The section featuring the overall highest
279 $^{231}\text{Pa}/^{230}\text{Th}$ corresponds to the LGM (around 29 cm) and is characterized by a massive change in
280 sedimentary composition as well as in the environmental boundary conditions. Due to the high
281 abundances of preserved foraminifera and high IRD counts, a certain particle effect on the ^{231}Pa
282 scavenging behavior cannot be excluded but is considered to be of subordinate relevance since these
283 particle types are not of primary importance for the scavenging of protactinium (Chase et al. 2004).

284 **4.3. The effect of sediment winnowing on $^{231}\text{Pa}/^{230}\text{Th}$**

285 For large parts of the $^{231}\text{Pa}/^{230}\text{Th}$ profile the sediment core experienced enhanced sediment winnowing
286 (Fig. 5c). Hence, besides the particle type also effects of sediment sorting and selective removal of
287 different sediment phases and grain sizes may have influenced the measured sedimentary $^{231}\text{Pa}/^{230}\text{Th}$
288 ratio (Geibert and Usbeck, 2004; Kretschmer et al., 2010; Kretschmer et al., 2011). Kretschmer et al.
289 (2011) investigated the effect of winnowing (removal) of the fine fraction ($< 20 \mu\text{m}$) with and without
290 opal-rich particles on the retained sedimentary $^{231}\text{Pa}/^{230}\text{Th}$ ratio, since protactinium is characterized by
291 a high affinity to particles built up from biogenic opal while thorium is preferentially scavenged by fine
292 sized particles like clay (e.g. Chase et al., 2002; Geibert and Usbeck, 2004; Rutgers van der Loeff et al.,
293 2016). From opal-rich sediments in the Southern Ocean Kretschmer et al. (2011) found that the
294 removal of the fine fraction ($< 20 \mu\text{m}$) alone would result in a slightly increased sedimentary $^{231}\text{Pa}/^{230}\text{Th}$
295 ratio since the lost fine particles like clay are a major carrier phase of scavenged ^{230}Th . In contrast, if
296 opal-rich particles, the main carrier phase of scavenged ^{231}Pa , is lost by winnowing the retained
297 $^{231}\text{Pa}/^{230}\text{Th}$ ratio can clearly decrease (Kretschmer et al., 2011 and their Fig. 4). Indeed, SU90-I02 shows
298 sediment winnowing prior the Holocene (Fig. 5c) a period which exhibited low $^{231}\text{Pa}/^{230}\text{Th}$ markedly
299 below the production ratio. However, since the sedimentary setting of SU90-I02 with its very low opal
300 concentrations (Fig. 3) is very different to the Southern Ocean, winnowing would rather have removed
301 ^{230}Th rich clay particles which should be evident in high $^{231}\text{Pa}/^{230}\text{Th}$. This is not observed here with
302 exception of a short excursion during the LGM. While this excursion could be explained by the removal
303 of clay particles it contradicts the observation of generally low $^{231}\text{Pa}/^{230}\text{Th}$ during strong winnowing.
304 Correlations between winnowing and $^{231}\text{Pa}/^{230}\text{Th}$ are thus considered too ambiguous for explaining the
305 observed variations in $^{231}\text{Pa}/^{230}\text{Th}$. Furthermore, the effect of sediment sorting on $^{231}\text{Pa}/^{230}\text{Th}$ has not
306 been observed yet for winnowing sites and is inferred from findings of Southern Ocean sediments
307 (Kretschmer et al., 2011).

308

309 From the observations as outlined in paragraph 4.2. and 4.3. it is concluded that the main features of
 310 the $^{231}\text{Pa}/^{230}\text{Th}$ record of SU90-I02 and the huge variations in absolute $^{231}\text{Pa}/^{230}\text{Th}$ values cannot have
 311 been primarily controlled by variations in particle fluxes, particle compositions or winnowing, but are
 312 best explained by large-scale AMOC variations imprinted in the sedimentary $^{231}\text{Pa}/^{230}\text{Th}$. The
 313 uncorrelated or even anti-correlated evolution of $^{231}\text{Pa}/^{230}\text{Th}$ with sediment fluxes in turn points
 314 towards variations in both $^{231}\text{Pa}/^{230}\text{Th}$ and sedimentation history along with changes in the circulation
 315 regime.



316
 317 **Fig. 5** The $^{231}\text{Pa}/^{230}\text{Th}$ (a) record of SU90-I02 compared to the ^{230}Th normalized sediment flux given in $\text{g}/\text{cm}^2/\text{ka}$ (b) and the
 318 sediment focusing factor Ψ (c) calculated from $^{230}\text{Th}_{\text{xso}}$ concentrations (Francois et al., 2004). High sediment fluxes
 319 correlated with the $^{231}\text{Pa}/^{230}\text{Th}$ activity ratios, indicative for a subordinate effect of the sediment flux on sedimentary
 320 $^{231}\text{Pa}/^{230}\text{Th}$. The dashed line in panel (a) indicates the production ratio of $^{231}\text{Pa}/^{230}\text{Th}$. The brown bar (hiatus) delineates the
 321 missing interval of the Deglacial in SU90-I02. The dashed line in panel (c) indicates a focusing factor of one which would
 322 indicate that now sediment is transported to or from this site. The strongest winnowing (sediment removal) is observed
 323 during the period of the proposed hiatus and is therefore in accordance with this finding.

324 **4.4. The SU90-I02 $^{231}\text{Pa}/^{230}\text{Th}$ record interpreted in terms of reflecting AMOC variations**

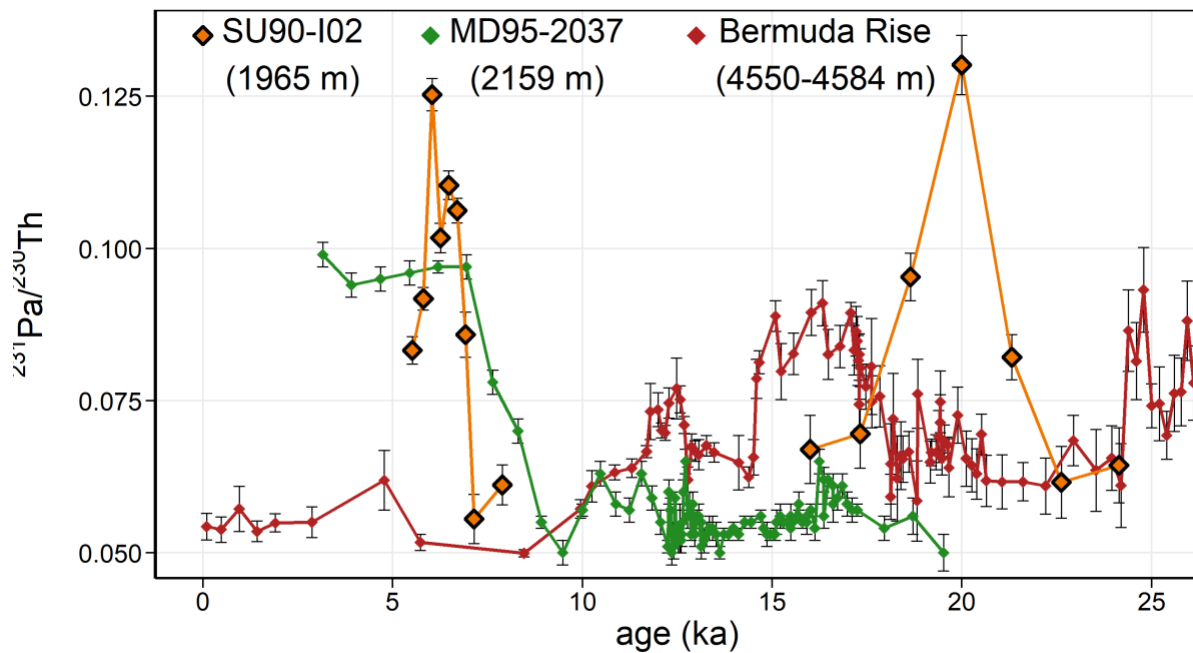
325 The here observed pattern of high Holocene and low Heinrich Stadial 1 and 2 $^{231}\text{Pa}/^{230}\text{Th}$ ratios is
326 inverted and at first glance contradicting compared to the prominent $^{231}\text{Pa}/^{230}\text{Th}$ profiles from the deep
327 northwestern Atlantic below 3000 m water depth (e.g. from the Bermuda Rise: McManus et al., 2004;
328 Blake-Bahama Outer Ridge: Süfke et al., 2019; Ceara Rise: Lippold et al., 2016; Ng et al., 2018;
329 Researchers Ridge: Ng et al., 2018) and time slice integrating compilations (Lippold et al., 2012a;
330 Bradtmiller et al., 2014; Burckel et al., 2016).

331 However, the course of the SU90-I02 $^{231}\text{Pa}/^{230}\text{Th}$ matches the general glacial to Holocene evolution
332 recorded by mid-depth North Atlantic site MD95-2037 at 2159 m (Gherardi et al., 2009; Fig. 1, 6). Both
333 cores from shallower water depths share the same general pattern in their $^{231}\text{Pa}/^{230}\text{Th}$ profile with low
334 values during prolonged cold periods (e.g. Heinrich Stadials) and a sharp increase to high Holocene
335 values at ~ 8 ka. This pattern is inverted to the $^{231}\text{Pa}/^{230}\text{Th}$ profiles from the deep northwestern Atlantic
336 (McManus et al., 2004; Lippold et al., 2009; Fig. 6) (low Holocene – high Glacial). Furthermore, the
337 timing of the early Holocene circulation change is earlier (between 11 to 10 ka) in the deep compared
338 the mid-depth Atlantic (see paragraph 4.5.; Fig. 6).

339 The position of a sediment core within one distinct overturning cell (in particular in terms of water
340 depth) has been identified as a crucial parameter for $^{231}\text{Pa}/^{230}\text{Th}$, as suggested by simple box model
341 approaches and observations (Luo et al., 2010; Lippold et al., 2011; Lippold et al., 2012a; Burckel et al.,
342 2016). Further, the depth dependency of $^{231}\text{Pa}/^{230}\text{Th}$ is amplified with increasing circulation strength.
343 A hypothetical static ocean would generate $^{231}\text{Pa}/^{230}\text{Th}$ deviations from the production ratio only due
344 to large-scale diffusion caused by gradients in the particle fluxes between the margins and the inner
345 ocean (boundary scavenging; Anderson et al., 1983; Hayes et al., 2015). But under a strong advection
346 regime low $^{231}\text{Pa}/^{230}\text{Th}$ in deep waters predominantly result from the increasing vertically integrated
347 deficit of ^{231}Pa relative to ^{230}Th . In shallower waters this deficit cannot build up efficiently due to the
348 smaller water column above. Instead, dissolved ^{231}Pa is supplied from upstream while ^{230}Th is
349 effectively scavenged to deeper waters leading to the observed decrease of $^{231}\text{Pa}/^{230}\text{Th}$ with water
350 depth. However, shallower water depths alone seem not to be a sufficient condition for high
351 $^{231}\text{Pa}/^{230}\text{Th}$. The Holocene $^{231}\text{Pa}/^{230}\text{Th}$ record at the Carolina Slope in a water depth of 1790 m (core
352 KN140-2-51 GGC in the direct flow path of the Atlantic Deep Western Boundary Current; Hoffmann et
353 al., 2018) displays constant values around 0.075 not exceeding the production ratio.

354 With adding this new mid-depth $^{231}\text{Pa}/^{230}\text{Th}$ record and reviewing the up-to-date available data base
355 (McManus et al., 2004; Gherardi et al., 2009; Lippold et al., 2009,2011,2012a,2016; Bradtmiller et al.,
356 2014; Böhm et al., 2015; Henry et al., 2016; Voigt et al., 2017; Mulitza et al., 2017; Ng et al., 2018;

357 Waelbroeck et al., 2018; Hoffmann et al., 2019; Süfke et al., 2019) on sedimentary $^{231}\text{Pa}/^{230}\text{Th}$ records
 358 from the western Atlantic, it becomes clear that even for a relatively constant mode of AMOC (as e.g.
 359 for the late Holocene) sedimentary $^{231}\text{Pa}/^{230}\text{Th}$ varies widely as a function of core location. As a
 360 consequence, predicting the behavior of $^{231}\text{Pa}/^{230}\text{Th}$ from a distinct position within a certain AMOC
 361 regime is unfortunately less intuitive. Accordingly, the use of adequate model approaches is necessary
 362 in order to better interpret $^{231}\text{Pa}/^{230}\text{Th}$ records (Luo et al., 2010; Rempfer et al., 2017).



363

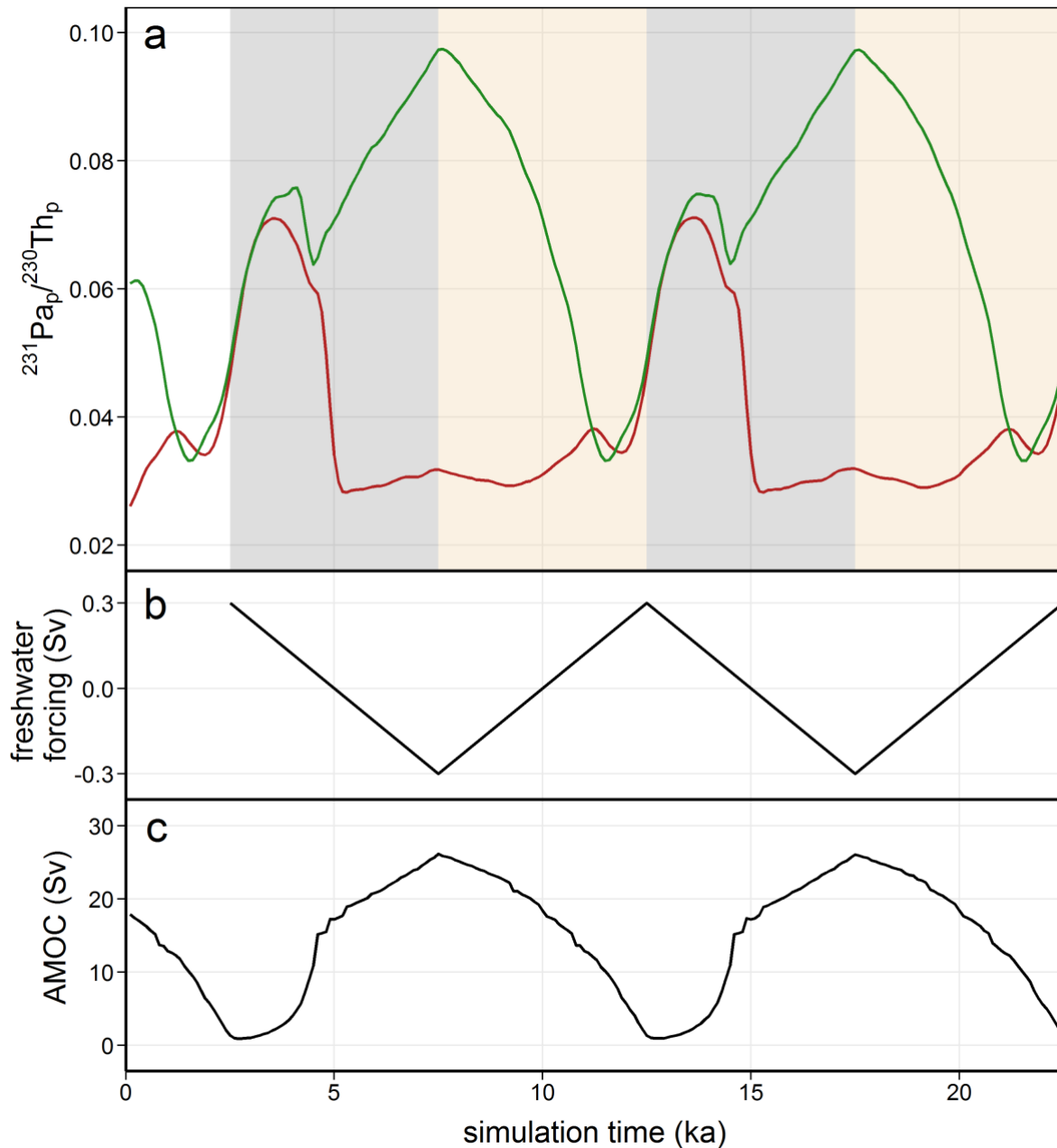
364 **Fig. 6** $^{231}\text{Pa}/^{230}\text{Th}$ profiles of SU90-I02, MD95-2037 (Gherardi et al., 2009) and the Bermuda Rise (McManus et al., 2004;
 365 Lippold et al., 2009).

366 **4.5. Modeled versus observed $^{231}\text{Pa}/^{230}\text{Th}$ at the mid-depth North Atlantic**

367 There have been model approaches clearly pointing towards the importance of the core location on
 368 $^{231}\text{Pa}/^{230}\text{Th}$ (Siddall et al., 2007; Luo et al., 2010; Lippold et al., 2012; Rempfer et al., 2017; Van Hulst
 369 et al., 2018), but the observational $^{231}\text{Pa}/^{230}\text{Th}$ data hardly reaches the required coverage for
 370 unambiguous AMOC reconstructions.

371 With the Bern3D Earth System Model Rempfer et al. (2017) showed in transient experiments, in which
 372 the strength of the AMOC has been varied by changing freshwater forcing, a strong statistical anti-
 373 correlation between variations in AMOC strength and the particle-bound $^{231}\text{Pa}_p/^{230}\text{Th}_p$ in great depths
 374 in the Northwest Atlantic region (i.e. low AMOC produces high $^{231}\text{Pa}/^{230}\text{Th}$ and vice versa; Fig. 7). The
 375 authors improved the simulation of the protactinium and thorium cycle from older versions by taking
 376 additional sink processes into account (bottom scavenging; boundary scavenging; with/without
 377 particle redissolution at depth). They found the relationship between AMOC and $^{231}\text{Pa}/^{230}\text{Th}$ to be

378 robust across these parametrizations, indicating that on larger spatial and temporal scales the
 379 relationship between $^{231}\text{Pa}/^{230}\text{Th}$ and AMOC is not fundamentally affected by uncertainties in the sink
 380 processes (e.g. bottom/boundary scavenging).



381

382 **Fig. 7** (a) Bern3D model output of the $^{231}\text{Pa}/^{230}\text{Th}$ signal from simulation Re3d_Bd_Fw of Rempfer et al. (2017) for the grid
 383 cells closest to the core location of SU90-102 (green) and for the deeper Bermuda Rise (red), which is also called Northwest
 384 Atlantic in Rempfer et al. (2017). (b) Amplitude of the North Atlantic freshwater forcing used by Rempfer et al. (2017),
 385 which causes the AMOC to fluctuate between 2 and 25 Sv. (c) The AMOC periodically fluctuates between practically no
 386 AMOC (2 Sv; e.g. at 2.5 ka) and a strong AMOC (25 Sv; e.g. at 7.5 ka) with a 10 kyr period. Gray bars indicate periods of
 387 increased AMOC strength (decreasing freshwater forcing), while light brown bars indicate decreasing AMOC (increasing
 388 freshwater forcing). The supplementary Fig. S4 indicates the used grid cells and shows the sign of $^{231}\text{Pa}/^{230}\text{Th}$ response to
 389 AMOC in different regions throughout the whole North Atlantic.

390 While the authors put emphasis on comparing the model outputs to the large observational data base
391 available from the northwestern Atlantic (more specific the Bermuda Rise; McManus et al., 2004;
392 Lippold et al., 2009; Henry et al., 2016), their model also reproduced observational features in other
393 regions which have not yet received much attention. The figure 8a of Rempfer et al. (2017) shows a
394 section plot of the North Atlantic (water depth versus latitude) indicating the correlation between
395 AMOC strength and $^{231}\text{Pa}_p/^{230}\text{Th}_p$. For the northwestern Atlantic up to $\sim 40^\circ\text{N}$ and below ~ 2500 m water
396 depth the negative model correlation corresponds to the classical picture as found in the Bermuda Rise
397 sediment cores. Interestingly, for the region north of $\sim 40^\circ\text{N}$ and above ~ 2500 m water depth this
398 correlation becomes inverted (strong AMOC causes higher $^{231}\text{Pa}/^{230}\text{Th}$). In this way, the modelling
399 study of Rempfer et al. (2017) already predicted that sediment cores north of $\sim 40^\circ\text{N}$ should show a
400 pattern of $^{231}\text{Pa}/^{230}\text{Th}$ vs. AMOC opposite to the expected, just as the results present in this study for
401 core SU90-I02. For this study the model output of simulation Re3d_Bd_Fw of Rempfer et al. (2017)
402 was revisited (see their Table A2 for parameters) without running new simulations. Thus, the AMOC
403 fluctuations in our Figure 7c are equal to these presented in Rempfer et al. (2017) in their Figure 7a.
404 The location of SU90-I02 indeed reveals a pattern highly sensitive on AMOC strength but asynchronous
405 to the Bermuda Rise (Fig. 7). The main reason for this inverted behavior is grounded by the prevailing
406 effect of import of ^{231}Pa over ^{230}Th from the upstream deep water formation zones as seen from the
407 increase of $^{231}\text{Pa}_p$ with virtually unchanged $^{230}\text{Th}_p$ levels (Rempfer et al., 2017). Subsequently, further
408 downstream and with increasing depth the ^{231}Pa deficit takes control due to meridional advection.

409 Furthermore, the model predicts a different response time of $^{231}\text{Pa}/^{230}\text{Th}$ variations in the deep
410 (Bermuda Rise) and mid-depth Atlantic (e.g. SU90-I02) during increasing AMOC strength. After 2.5 ka
411 of decreasing freshwater forcing (after 5 ka of simulation time in Fig. 7) $^{231}\text{Pa}/^{230}\text{Th}$ in the deep Atlantic
412 reacts by a sharp decline from higher to lower values quickly reaching lowest levels which stays
413 constant even during ongoing freshwater forcing. In contrast, after transient concordant behavior the
414 mid-depth Atlantic shows a gradual increase in $^{231}\text{Pa}/^{230}\text{Th}$ after 2.5 ka of decreasing freshwater forcing
415 with overall highest values at the lowest point of freshwater forcing and therefore strongest AMOC.
416 This time lag between circulation change and $^{231}\text{Pa}/^{230}\text{Th}$ response at the mid-depth Atlantic compared
417 to the deep Atlantic is reflected by the patterns seen in SU90-I02 and MD95-2037. Both cores show
418 low $^{231}\text{Pa}/^{230}\text{Th}$ values during the early Holocene while the deep Atlantic already shows low $^{231}\text{Pa}/^{230}\text{Th}$
419 values (Fig. 6) indicating a strong circulation (the mid-depth cores are supposed to show high values
420 during a strong AMOC, Fig. S5). The time lag between decreasing $^{231}\text{Pa}/^{230}\text{Th}$ values in the deep Atlantic
421 and increasing values in the mid-depth Atlantic is in the order of 2-4 ka (Fig. 6) which is similar to the
422 model findings (Fig. 7). Therefore, the model findings do not only predicts the general direction of
423 $^{231}\text{Pa}/^{230}\text{Th}$ change under variations in AMOC strength at a given position in the West Atlantic
424 Overturning cell but also the relative timing.

425 **Conclusions**

426 Sedimentary analyses of the mid-depth North Atlantic core SU90-I02 result in a classical picture of IRD
427 dominated sediments for Heinrich Stadials 1 and 2. Changes in sedimentology corresponding to the
428 climatic periods of Heinrich Stadial 1 and 2, the LGM and the Holocene are clearly resolvable. The new
429 established $^{231}\text{Pa}/^{230}\text{Th}$ down core profile from SU90-I02 reveals $^{231}\text{Pa}/^{230}\text{Th}$ values higher than the
430 production ratio during periods of strong AMOC, such as the Holocene. The effect of the particle flux
431 and enhanced scavenging of protactinium is found minor during these periods. Hence, the sedimentary
432 $^{231}\text{Pa}/^{230}\text{Th}$ of this core at 45°N shows an opposite behavior compared to deep Atlantic sites (e.g. the
433 Bermuda Rise) with values clearly below the production ratio during cold phases, like Heinrich Stadials
434 1 and 2. However, findings from the Bern3D model (e.g. Rempfer et al., 2017) confirm such an
435 oppositional behavior in $^{231}\text{Pa}/^{230}\text{Th}$ between the deep northwestern and the mid-depth northern
436 Atlantic north of 40°N. This model predicts that $^{231}\text{Pa}/^{230}\text{Th}$ from mid-depth sites north of 40°N
437 correlate positively with the AMOC strength. This study adds a further downcore profile to the still
438 sparse Atlantic $^{231}\text{Pa}/^{230}\text{Th}$ data-base and highlights the importance of considering the core position for
439 interpretations of $^{231}\text{Pa}/^{230}\text{Th}$ ratios, even inside the same overturning cell. By combining spatially
440 distributed, well dated and synchronized $^{231}\text{Pa}/^{230}\text{Th}$ records in the Atlantic Ocean much tighter
441 constraints can be placed on changes in deep ocean circulation pathways and water mass distributions.

442 **Acknowledgment**

443 We thank Isabelle Billy from the University of Bordeaux and Claire Waelbroeck and Elisabeth Michel
444 from the LSCE in Paris for providing the samples of SU90-I02 for the $^{231}\text{Pa}/^{230}\text{Th}$ and XRF analysis. XRF
445 measurements were supported by Andreas Koutsodendris and Siphon de Finès was always supportive
446 during laboratory work. We acknowledge the constructive comments of two anonymous reviewers.
447 This study has been funded by the Emmy-Noether-Programm of the German Research Foundation
448 (DFG) Grant Li1815/4.

449 **References**

- 450 Anderson RF, Bacon MP, Brewer PG (1983) Removal of ^{230}Th and ^{231}Pa at ocean margins. *Earth*
451 *Planet Sci Lett* 66:73–90. doi: 10.1016/0012-821X(83)90127-9
- 452 Andrews JT, Tedesco K (1992) Detrital carbonate-rich sediments, northwestern Labrador Sea:
453 implications for ice-sheet dynamics and iceberg rafting (Heinrich) events in the North Atlantic.
454 *Geology* 20:1087–1090. doi: 10.1130/0091-7613(1992)020<1087:DCRSNL>2.3.CO;2
- 455 Andrews JT, Voelker AHL (2018) “Heinrich events” (& sediments): A history of terminology and
456 recommendations for future usage. *Quat Sci Rev* 187:31–40. doi: 10.1016/j.quascirev.2018.03.017

457 Bandy OL (1972) Origin and Development of Globorotalia (Turborotalia) pachyderma (Ehrenberg).
458 *Micropaleontology* 18:294. doi: 10.2307/1485010

459 Banner FT, Blow WH (1960) Some primary types of species belonging to the superfamily
460 Globigerinaceae. *Contrib from Cushman Found Foraminifer Res* 11:1–41

461 Böhm E, Lippold J, Gutjahr M, et al (2015) Strong and deep Atlantic meridional overturning
462 circulation during the last glacial cycle. *Nature* 517:73–76. doi: 10.1038/nature14059

463 Bond G, Heinrich H, Broecker W, et al (1992) Evidence for massive discharges of icebergs into the
464 North Atlantic ocean during the last glacial period. *Nature* 360:245–249. doi: 10.1038/360245a0

465 Bradtmiller LI, McManus JF, Robinson LF (2014) 231Pa/230Th evidence for a weakened but persistent
466 Atlantic meridional overturning circulation during Heinrich Stadial 1. *Nat Commun* 5:5817. doi:
467 10.1038/ncomms6817

468 Broecker W, Bond G, Klas M, Clark E, McManus J (1992) Origin of the northern Atlantic's Heinrich
469 events. *Climate Dynamics* 6:265–273. doi: 10.1007/BF00193540

470 Broecker WS, Bond G, Klas M (1990) A salt oscillator in the glacial Atlantic. *Paleoceanography* 5:469–
471 477. doi: 10.1029/PA005i004p00469

472 Burckel P, Waelbroeck C, Luo Y, et al (2016) Changes in the geometry and strength of the Atlantic
473 meridional overturning circulation during the last glacial (20–50 ka). *Clim Past* 12:2061–2075. doi:
474 10.5194/cp-12-2061-2016

475 Chase Z, Anderson RF, Fleisher MQ, Kubik PW (2002) The influence of particle composition and
476 particle flux on scavenging of Th, Pa and Be in the ocean. *Earth Planet Sci Lett* 204:215–229. doi:
477 10.1016/S0012-821X(02)00984-6

478 Chase Z, Anderson RF, Fleisher MQ, Kubik PW (2003) Scavenging of 230Th, 231Pa and 10Be in the
479 Southern Ocean (SW Pacific sector): The importance of particle flux, particle composition and
480 advection. *Deep Res Part II Top Stud Oceanogr* 50:739–768. doi: 10.1016/S0967-0645(02)00593-3

481 Chase Z, Anderson RF (2004) Comment on “On the importance of opal, carbonate, and lithogenic
482 clays in scavenging and fractionating 230 Th, 231 Pa and 10 Be in the ocean” by S. Luo and T.-L. Ku.
483 *Earth Planet Sci Lett* 220:213–222. doi: 10.1016/S0012-821X(04)00028-7

484 Christl M, Lippold J, Hofmann A, et al (2010) 231Pa/230Th: A proxy for upwelling off the coast of
485 West Africa. *Nucl Instruments Methods Phys Res Sect B Beam Interact with Mater Atoms* 268:1159–
486 1162. doi: 10.1016/j.nimb.2009.10.123

487 Clark PU, Marshall SJ, Clarke GKS, et al (2001) Freshwater Forcing of Abrupt Climate Change During
488 the Last Glaciation. *Science* 293:283–287. doi: 10.1126/science.1062517

489 Duplessy JC, Labeyrie L, Arnold M, et al (1992) Changes in surface salinity of the North Atlantic Ocean
490 during the last deglaciation. *Nature* 358:485–488. doi: 10.1038/358485a0

491 Ferreira ML de C, Kerr R (2017) Source water distribution and quantification of North Atlantic Deep
492 Water and Antarctic Bottom Water in the Atlantic Ocean. *Prog Oceanogr* 153:66–83. doi:
493 10.1016/j.pocean.2017.04.003

494 Fietzke J, Bollhöfer A, Frank M, Mangini A (1999) Protactinium determination in manganese crust
495 VA13/2 by thermal ionization mass spectrometry (TIMS). *Nucl Instruments Methods Phys Res Sect B*
496 *Beam Interact with Mater Atoms* 149:353–360. doi: 10.1016/S0168-583X(98)00912-4

497 Francois R, Frank M, Rutgers van der Loeff MM, Bacon MP (2004) 230 Th normalization: An essential
498 tool for interpreting sedimentary fluxes during the late Quaternary. *Paleoceanography* 19. doi:
499 10.1029/2003PA000939

500 Geibert W, Usbeck R (2004) Adsorption of thorium and protactinium onto different particle types:
501 Experimental findings. *Geochim Cosmochim Acta* 68:1489–1501. doi: 10.1016/j.gca.2003.10.011

502 Gherardi JM, Labeyrie L, McManus JF, et al (2005) Evidence from the Northeastern Atlantic basin for
503 variability in the rate of the meridional overturning circulation through the last deglaciation. *Earth*
504 *Planet Sci Lett* 240:710–723. doi: 10.1016/j.epsl.2005.09.061

505 Gherardi JM, Labeyrie L, Nave S, et al (2009) Glacial-interglacial circulation changes inferred
506 from 231Pa/ 230Th sedimentary record in the North Atlantic region. *Paleoceanography* 24:1–14. doi:
507 10.1029/2008PA001696

508 Gottschalk J, Szidat S, Michel E, et al (2018) Radiocarbon measurements of small-size foraminiferal
509 samples with the MIni CARbon DAting System (MICADAS) at the University of Bern: implications for
510 paleoclimate reconstructions. *Radiocarbon* 60:469-491. doi: 10.1017/RDC.2018.3

511 Grousset FE, Cortijo E, Huon S, et al (2001) Zooming in on Heinrich layers. *Paleoceanography* 16:240–
512 259. doi: 10.1029/2000PA000559

513 Gu S, Liu Z (2017) 231Pa and 230Th in the ocean model of the Community Earth System Model
514 (CESM1.3). *Geosci Model Dev* 10:4723–4742. doi: 10.5194/gmd-10-4723-2017

515 Hall IR, Moran SB, Zahn R, et al (2006) Accelerated drawdown of meridional overturning in the late-
516 glacial Atlantic triggered by transient pre-H event freshwater perturbation. *Geophys Res Lett* 33:1–5.
517 doi: 10.1029/2006GL026239

518 Hayes CT, Anderson RF, Fleisher MQ, et al (2015a) 230Th and 231Pa on GEOTRACES GA03, the U.S.
519 GEOTRACES North Atlantic transect, and implications for modern and paleoceanographic chemical
520 fluxes. *Deep Res Part II Top Stud Oceanogr* 116:29–41. doi: 10.1016/j.dsr2.2014.07.007

521 Hayes CT, Anderson RF, Fleisher MQ, et al (2015b) Intensity of Th and Pa scavenging partitioned by
522 particle chemistry in the North Atlantic Ocean. *Mar Chem* 170:49–60. doi:
523 10.1016/j.marchem.2015.01.006

524 Heinrich H (1988) Origin and Consequences of Cyclic Ice Rafting in the Northeast Atlantic Ocean
525 during the Past 130,000 Years. *Quat Res* 29:142–152. doi: 10.1016/0033-5894(88)90057-9

526 Hemming SR (2004) Heinrich events: Massive late Pleistocene detritus layers of the North Atlantic
527 and their global climate imprint. *Rev Geophys* 42:1-43. doi: 10.1029/2003RG000128

528 Henderson GM, Anderson RF (2003) The U-series Toolbox for Paleoceanography. *Rev Mineral*
529 *geochemistry* 52:493–531. doi: 10.2113/0520493

530 Henry LG, McManus JF, Curry WB, et al (2016) North Atlantic ocean circulation and abrupt climate
531 change during the last glaciation. *Science* 353:470–474. doi: 10.1126/science.aaf5529

532 Hodell DA, Channeil JET, Curtis JH, et al (2008) Onset of “Hudson Strait” Heinrich events in the
533 eastern North Atlantic at the end of the middle Pleistocene transition (~640 ka)? *Paleoceanography*
534 23:1–16. doi: 10.1029/2008PA001591

535 Hodell DA, Nicholl JA, Bontognali TRR, et al (2017) Anatomy of Heinrich Layer 1 and its role in the last
536 deglaciation. *Paleoceanography* 32:284–303. doi: 10.1002/2016PA003028

537 Hoffmann SS, McManus JF, Swank E. (2018) Evidence for Stable Holocene Basin-Scale Overturning
538 Circulation Despite Variable Currents Along the Deep Western Boundary of the North Atlantic Ocean.
539 *Geophys Res Lett* 45:1–10. doi: 10.1029/2018GL080187

540 Jullien E, Grousset FE, Hemming SR, et al (2006) Contrasting conditions preceding MIS3 and MIS2
541 Heinrich events. *Glob Planet Change* 54:225–238. doi: 10.1016/j.gloplacha.2006.06.021

542 Kretschmer S, Geibert W, Rutgers van der Loeff MM, et al (2011) Fractionation of 230Th, 231Pa, and
543 10Be induced by particle size and composition within an opal-rich sediment of the Atlantic Southern
544 Ocean. *Geochim Cosmochim Acta* 75:6971–6987. doi: 10.1016/j.gca.2011.09.012

545 Kretschmer S, Geibert W, Rutgers van der Loeff MM, Mollenhauer G (2010) Grain size effects on 230
546 Thxs inventories in opal-rich and carbonate-rich marine sediments. *Earth Planet Sci Lett* 294:131–
547 142. doi: 10.1016/j.epsl.2010.03.021

548 Kucera M (2007) Chapter Six Planktonic Foraminifera as Tracers of Past Oceanic Environments. *Dev Mar Geol* 1:213–262. doi: 10.1016/S1572-5480(07)01011-1

549 Labeyrie AL, Vidal L, Cortijo E, et al (1995) Surface and deep hydrology of the Northern Atlantic Ocean
550 during the past 150000 years. *Philos Trans R Soc London Ser B Biol Sci* 348:255–264. doi:
551 10.1098/rstb.1995.0067

552 Lambelet M, van de Flierdt T, Crocket K, et al (2016) Neodymium isotopic composition and
553 concentration in the western North Atlantic Ocean: Results from the GEOTRACES GA02 section.
554 *Geochim Cosmochim Acta* 177:1–29. doi: 10.1016/j.gca.2015.12.019

555 Lippold J, Grützner J, Winter D, et al (2009) Does sedimentary $^{231}\text{Pa}/^{230}\text{Th}$ from the Bermuda Rise
556 monitor past Atlantic Meridional Overturning Circulation? *Geophys Res Lett* 36:1–6. doi:
557 10.1029/2009GL038068

558 Lippold J, Gherardi JM, Luo Y (2011) Testing the $^{231}\text{Pa}/^{230}\text{Th}$ paleocirculation proxy: A data versus
559 2D model comparison. *Geophys Res Lett* 38:1–7. doi: 10.1029/2011GL049282

560 Lippold J, Luo Y, Francois R, et al (2012a) Strength and geometry of the glacial Atlantic Meridional
561 Overturning Circulation. *Nat Geosci* 5:813–816. doi: 10.1038/ngeo1608

562 Lippold J, Mulitza S, Mollenhauer G, et al (2012b) Boundary scavenging at the East Atlantic margin
563 does not negate use of $^{231}\text{Pa}/^{230}\text{Th}$ to trace Atlantic overturning. *Earth Planet Sci Lett* 333–
564 334:317–331. doi: 10.1016/j.epsl.2012.04.005

565 Lippold J, Gutjahr M, Blaser P, et al (2016) Deep water provenance and dynamics of the (de)glacial
566 Atlantic meridional overturning circulation. *Earth Planet Sci Lett* 445:68–78. doi:
567 10.1016/j.epsl.2016.04.013

568 Luo Y, Francois R, Allen S (2010) Sediment $^{231}\text{Pa}/^{230}\text{Th}$ as a recorder of the rate of the Atlantic
569 meridional overturning circulation: insights from a 2-D model. *Ocean Sci* 6:381–400. doi: 10.5194/os-
570 6-381-2010

571 Lynch-Stieglitz J (2017) The Atlantic Meridional Overturning Circulation and Abrupt Climate Change.
572 *Ann Rev Mar Sci* 9:83–104. doi: 10.1146/annurev-marine-010816-060415

573 Manighetti B, McCave IN, Maslin M, Shackleton NJ (1995) Chronology for climate change: Developing
574 age models for the biogeochemical ocean flux study cores. *Paleoceanography* 10:513–525. doi:
575 10.1029/94PA03062

576 Marchal O, Francois R, Stocker TF, Joos F (2000) Ocean thermohaline circulation and sedimentary
577 $^{231}\text{Pa}/^{230}\text{Th}$ ratio. *Paleoceanography* 15:625–641. doi: 10.1029/2000PA000496

578 McManus JF, Francois R, Gherardi J-M, et al (2004) Collapse and rapid resumption of Atlantic
579 meridional circulation linked to deglacial climate changes. *Nature* 428:834–837. doi:
580 10.1038/nature02494

581 Missiaen L, Pichat S, Waelbroeck C, et al (2018) Downcore Variations of Sedimentary Detrital
582 (238U/232Th) Ratio: Implications on the Use of 230Th and 231Pa to Reconstruct Sediment Flux and
583 Ocean Circulation. *Geochemistry, Geophysics Geosystems* 19:2560–2573. doi: 10.1029/2017GC007410

584 Mulitza S, Chiessi CM, Schefuß E, et al (2017) Synchronous and proportional deglacial changes in
585 Atlantic meridional overturning and northeast Brazilian precipitation. *Paleoceanography* 32:622–633.
586 doi: 10.1002/2017PA003084

587 Müller PJ, Schneider R (1993) An automated leaching method for the determination of opal in
588 sediments and particulate matter. *Deep Res Part I* 40:425–444. doi: 10.1016/0967-0637(93)90140-X

589 Ng HC, Robinson LF, McManus JF, et al (2018) Coherent deglacial changes in western Atlantic Ocean
590 circulation. *Nat Commun* 9:1–10. doi: 10.1038/s41467-018-05312-3

591 Pham MK, Sanchez-Cabeza JA, Povinec PP, et al (2008) A new Certified Reference Material for
592 radionuclides in Irish sea sediment (IAEA-385). *Appl Radiat Isot* 66:1711–1717. doi:
593 10.1016/j.apradiso.2007.10.020

594 Rashid H, Boyle EA (2007) Mixed-Layer Deepening During Heinrich Events : A Multi-Planktonic
595 Foraminiferal $\delta^{18}\text{O}$ Approach. *Science* 318:439–441. doi: 10.1126/science.1146138

596 Reimer PJ, Bard E, Bayliss A, et al. (2013) IntCal13 and Marine13 radiocarbon age calibration curves 0-
597 50,000 years cal BP. *Radiocarbon* 55:1869-1887. doi: 10.2458/azu_js_rc.55.16947

598 Regelous M, Turner SP, Elliott TR, et al (2004) Measurement of femtogram quantities of protactinium
599 in silicate rock samples by multicollector inductively coupled plasma mass spectrometry. *Anal Chem*
600 76:3584–3589. doi: 10.1021/ac030374l

601 Rempfer J, Stocker TF, Joos F, et al (2017) New insights into cycling of 231 Pa and 230 Th in the
602 Atlantic Ocean. *Earth Planet Sci Lett* 468:27–37. doi: 10.1016/j.epsl.2017.03.027

603 Roberts NL, McManus JF, Piotrowski AM, McCave IN (2014) Advection and scavenging controls of
604 Pa/Th in the northern NE Atlantic. *Paleoceanography* 29:668–679. doi: 10.1002/2014PA002633

605 Roche D, Paillard D, Cortijo E (2004) Constraints on the duration and freshwater release of Heinrich
606 event 4 through isotope modelling. *Nature* 432:379–382. doi: 10.1038/nature03059

607 Ruddiman WF (1977) North atlantic ice-rafting: A major change at 75,000 years before the present.
608 Science 196:1208–1211. doi: 10.1126/science.196.4295.1208

609 Rutgers van der Loeff M, Venchiarutti C, Stimac I, et al (2016) Meridional circulation across the
610 Antarctic Circumpolar Current serves as a double ^{231}Pa and ^{230}Th trap. Earth Planet Sci Lett 455:73–
611 84. doi: 10.1016/j.epsl.2016.07.027

612 Schiebel R and Hemleben C (2017). Planktic Foraminifera in the Modern Ocean. Springer, Berlin
613 Heidelberg 333pp. ISBN 978-3-662-50297-6

614 Schulz H (1995a) Planktic foraminifera assemblage in sediment core SU90-I02. Pangaea. doi:
615 10.1594/PANGAEA.134148

616 Schulz H (1995b) Stable isotope analysis on planktic foraminifera in sediment core SU90-I02.
617 Pangaea. doi: 10.1594/PANGAEA.107750

618 Siddall M, Stocker TF, Henderson GM, et al (2007) Modeling the relationship between $^{231}\text{Pa}/^{230}\text{Th}$
619 distribution in North Atlantic sediment and Atlantic meridional overturning circulation.
620 Paleoceanography 22:1–14. doi: 10.1029/2006PA001358

621 Storz D, Schulz H, Waniek JJ, et al (2009) Seasonal and interannual variability of the planktic
622 foraminiferal flux in the vicinity of the Azores Current. Deep Res Part I Oceanogr Res Pap 56:107–124.
623 doi: 10.1016/j.dsr.2008.08.009

624 Sűfke F, Lippold J, Happel S (2018) Improved Separation of Pa from Th and U in Marine Sediments
625 with TK400 Resin. Anal Chem 90:1395–1401. doi: 10.1021/acs.analchem.7b04723

626 Sűfke F, Pöppelmeier F, Goepfert TJ, et al (2019) Constraints on the northwestern Atlantic deep
627 water circulation from $^{231}\text{Pa}/^{230}\text{Th}$ during the last 30,000 years. Paleoceanography and
628 Paleoclimatology (accepted). doi: 10.1029/2019PA003737

629 Szidat S, Salazar GA, Vogel E, et al (2014) ^{14}C analysis and sample preparation at the new Bern
630 Laboratory for the Analysis of Radiocarbon with AMS (LARA). Radiocarbon 56:561–566. doi:
631 10.2458/56.17457

632 Waelbroeck C, Pichat S, Böhm E, et al (2018) Relative timing of precipitation and ocean circulation
633 changes in the western equatorial Atlantic over the last 45 kyr. Clim Past 14:1315–1330. doi:
634 10.5194/cp-14-1315-2018

635 Watkins SJ, Maher BA, Bigg GR (2007) Ocean circulation at the Last Glacial Maximum: A combined
636 modeling and magnetic proxy-based study. Paleoceanography 22:1–20. doi: 10.1029/2006PA001281

- 637 Van Hulst M, Dutay JC, Roy-Barman M (2018) A global scavenging and circulation ocean model of
638 thorium-230 and protactinium-231 with improved particle dynamics (NEMO-ProThorP 0.1). *Geosci*
639 *Model Dev* 11:3537–3556. doi: 10.5194/gmd-11-3537-2018
- 640 Voigt I, Cruz APS, Mulitza S, et al (2017) Variability in mid-depth ventilation of the western Atlantic
641 Ocean during the last deglaciation. *Paleoceanography* 1–18. doi: 10.1002/2017PA003095
- 642 Yu E-F, Francois R, Bacon MP (1996) Similar rates of modern and last-glacial ocean thermohaline
643 circulation inferred from radiochemical data. *Nature* 379:689–694. doi: 10.1038/379689a0